J|A|C|S ARTICLES

Published on Web 05/25/2010

Chirality and Electronic Structure of the Thiolate-Protected Au_{38} Nanocluster

Olga Lopez-Acevedo,[†] Hironori Tsunoyama,[‡] Tatsuya Tsukuda,[‡] Hannu Häkkinen,[†,§] and Christine M. Aikens*,[||]

Department of Physics, Nanoscience Center, University of Jyväskylä, FI-40014 Jyväskylä, Finland, Catalysis Research Center, Hokkaido University, Nishi 10, Kita 21, Sapporo 001-0021, Japan, Department of Chemistry, Nanoscience Center, University of Jyväskylä, FI-40014 Jyväskylä, Finland, and Department of Chemistry, Kansas State University, Manhattan, Kansas 66506

Received April 7, 2010; E-mail: cmaikens@ksu.edu

Abstract: Structural, electronic, and optical properties of the thiolate-protected $Au_{38}(SR)_{24}$ cluster are studied by density-functional theory computations ($R = CH_3$ and $R = C_6H_{13}$) and by powder X-ray crystallography ($R = C_{12}H_{25}$). A low-energy structure which can be written as $Au_{23}@(Au(SR)_2)_3(Au_2(SR)_3)_6$ having a bicosahedral core and a *chiral arrangement* of the protecting gold−thiolate $Au_x(SR)_y$ units yields an excellent match between the computed (for $R = C_6H_{13}$) and measured (for $R = C_{12}H_{25}$) powder X-ray diffraction function. We interpret in detail the electronic structure of the Au_{23} core by using a particle-in-a-cylinder model. Although the alkane thiolate ligands are achiral, the chiral structure of the ligand layer yields strong circular dichroism (CD) in the excitations below 2.2 eV for $Au_{38}(SCH_3)_{24}$. Our calculated CD spectrum is in quantitative agreement with the previously measured low-energy CD signal of glutathione-protected $Au_{38}(SG)_{24}$. Our study demonstrates a new mechanism for the strong chiral response of thiolate-protected gold clusters with achiral metal cores and ligands.

Introduction

Ligand-protected gold nanoparticles have important applications in nanotechnology, biology, and catalysis,[1−10] including enantioselective catalysis.[11] Tremendous advances have been achieved in the synthesis and isolation of self-assembled thiolate-monolayer-protected clusters (SR-MPCs) in the 1−2 nm regime.[12−31] Achieving monodispersity in the sample preparation has allowed detailed characterizations of their size-dependent electronic, chemical, and spectral properties, such as highly structured (molecule-like) optical absorption spectra,

[†] Department of Physics, University of Jyväskylä.
[‡] Hokkaido University.
[§] Department of Chemistry, University of Jyväskylä.
[||] Kansas State University.

(1) (a) Whetten, R. L.; Khoury, J. T.; Alvarez, M. M.; Murthy, S.; Vezmar, I.; Wang, Z. L.; Stephens, P. W.; Cleveland, C. L.; Luedtke, W. D.; Landman, U. *Adv. Mater.* **1996**, *8*, 428. (b) Templeton, A. C.; Wuelfing, W. P.; Murray, R. W. *Acc. Chem. Res.* **2000**, *33*, 27. (c) Daniel, M.-C.; Astruc, D. *Chem. Rev.* **2004**, *104*, 293. (d) Brust, M.; Kiely, C. J. *Colloids Surf., A* **2002**, *202*, 175. (e) Sardart, R.; Funston, A. M.; Mulvaney, P.; Murray, R. W. *Langmuir* **2009**, *25*, 13840. (f) Elghanian, R.; Storhoff, J. J.; Mucic, R. C.; Letsinger, R. L.; Mirkin, C. A. *Science* **1997**, *277*, 1078. Chen, S.; Ingram, R. S.; Hostetler, M. J.; Pietron, J. J.; Murray, R. W.; Schaaff, T. G.; Khoury, J. T.; Alvarez, M. M.; Whetten, R. L. *Science* **1998**, *280*, 2098.
(2) Jahn, W. *J. Struct. Biol.* **1999**, *127*, 106.
(3) (a) El-Sayed, I. H.; Huang, X.; El-Sayed, M. A. *Nano Lett.* **2005**, *5*, 829. (b) Huang, X.; El-Sayed, I. H.; Qian, W.; El-Sayed, M. A. *J. Am. Chem. Soc.* **2006**, *128*, 2115.
(4) Bowman, M. C.; Ballard, T. E.; Ackerson, C. J.; Feldheim, D. L.; Margolis, D. M.; Melander, C. *J. Am. Chem. Soc.* **2008**, *130*, 6896.
(5) Haruta, M.; Yamada, N.; Kobayashi, T.; Iijima, S. *J. Catal.* **1989**, *115*, 301.
(6) (a) Tsunoyama, H.; Sakurai, H.; Negishi, Y.; Tsukuda, T. *J. Am. Chem. Soc.* **2005**, *127*, 9374. (b) Tsunoyama, H.; Sakurai, H.; Tsukuda, T. *Chem. Phys. Lett.* **2006**, *429*, 528.
(7) Lopez-Acevedo, O.; Kacprzak, K. A.; Akola, J.; Häkkinen, H. *Nat. Chem.* **2010**, *2*, 329.
(8) Chaki, N. K.; Tsunoyama, H.; Negishi, Y.; Sakurai, H.; Tsukuda, T. *J. Phys. Chem. C* **2007**, *111*, 4885.
(9) Han, J.; Liu, Y.; Guo, R. *J. Am. Chem. Soc.* **2009**, *131*, 2060.
(10) Zhu, Y.; Qian, H.; Drake, B. A.; Jin, R. *Angew. Chem., Int. Ed.* **2010**, *49*, 1295.
(11) Takizawa, S.; Patil, M. L.; Marubayashi, K.; Sasai, H. *Tetrahedron* **2007**, *63*, 6512.
(12) Negishi, Y.; Nobusada, K.; Tsukuda, T. *J. Am. Chem. Soc.* **2005**, *127*, 5261.
(13) Negishi, Y.; Tsunoyama, H.; Suzuki, M.; Kawamura, N.; Matsushita, M. M.; Maruyama, K.; Sugawara, T.; Yokoyama, T.; Tsukuda, T. *J. Am. Chem. Soc.* **2006**, *128*, 12034.
(14) Tsunoyama, H.; Negishi, Y.; Tsukuda, T. *J. Am. Chem. Soc.* **2006**, *128*, 6036.
(15) Shichibu, Y.; Negishi, Y.; Tsunoyama, H.; Kanehara, M.; Teranishi, T.; Tsukuda, T. *Small* **2007**, *3*, 835.
(16) Chaki, N. K.; Negishi, Y.; Tsunoyama, H.; Shichibu, Y.; Tsukuda, T. *J. Am. Chem. Soc.* **2008**, *130*, 8608.
(17) Zhu, M.; Lanni, E.; Garg, N.; Bier, M. E.; Jin, R. *J. Am. Chem. Soc.* **2008**, *130*, 1138–1139.
(18) Qian, H.; Zhu, M.; Anderson, U. N.; Jin, R. *J. Phys. Chem. A* **2009**, *113*, 4281.
(19) (a) Fields-Zinna, C. A.; Sardar, R.; Beasley, C. A.; Murray, R. W. *J. Am. Chem. Soc.* **2009**, *131*, 16266. (b) Qian, H.; Jin, R. *Nano Lett.* **2009**, *9*, 4083.
(20) Dass, A. *J. Am. Chem. Soc.* **2009**, *131*, 11666.
(21) (a) Qian, H.; Zhu, Y.; Jin, R. *ACS Nano* **2009**, *3*, 3795. (b) Qian, H.; Zhu, Y.; Jin, R. *J. Am. Chem. Soc.* **2010**, *132*, 4585.
(22) Wyrwas, R. B.; Alvarez, M. M.; Khoury, J. T.; Price, R. C.; Schaaff, T. G.; Whetten, R. L. *Eur. Phys. J. D* **2007**, *43*, 91.
(23) Alvarez, M. M.; Khoury, J. T.; Schaaff, T. G.; Shafigullin, M. N.; Vezmar, I.; Whetten, R. L. *J. Phys. Chem. B* **1997**, *101*, 3706.
(24) (a) Schaaff, T. G.; Shafigullin, M. N.; Khoury, J. T.; Vezmar, I.; Whetten, R. L.; Cullen, W. G.; First, P. N.; Gutiérrez-Wing, C.; Ascensio, J.; Jose-Yacamán, M. J. *J. Phys. Chem. B* **1997**, *101*, 7885. (b) Schaaff, T. G.; Whetten, R. L. *J. Phys. Chem. B* **2000**, *104*, 2630.

 10.1021/ja102934q

intense circular dichroism (CD), nonlinear optical properties, and photoluminescence. Certain particle sizes appear to be particularly stable ("magic") and can be selectively synthesized via core etching or kinetically controlled procedures, including $Au_{25}(SR)_{18}^{-1}$,[15,17] $Au_{38}(SR)_{24}$,[16,18,27] $Au_{68}(SR)_{34}$,[20] and the clusters $Au_{144-146}(SR)_{59-60}$.[16,19]

Using matrix-assisted laser desorption ionization coupled with mass spectrometry (MALDI-MS), Whetten and co-workers proposed over a decade ago that a nanoparticle with a core mass of ~8 kDa should have approximately 38 Au atoms and 24 thiolates.[24] In the following years, confusion arose in the literature when several studies examined clusters with an unknown composition with distinct molecular properties, labeling it as Au_{38}, now known to be $Au_{25}(SR)_{18}^{-1}$. However, in 2008, precise nondestructive electrospray ionization mass spectrometry (ESI-MS) experiments confirmed the assignment $Au_{38}(SR)_{24}$.[16] Recent HAADF-STEM experiments have also concluded that these nanoparticles contain 38 ± 2 Au atoms while supported by inert substrates.[26] Fingerprint characteristics have been determined from electrochemistry and optical experiments. From electrochemistry experiments, the HOMO−LUMO gap of this species is determined to be 0.9 eV and the estimated charge of the nanoparticle is zero.[1e,27,28] Optical absorption spectra show that the cluster has molecular-like electronic states in accordance with the results of electrochemical experiments. The optical spectrum shows strong low energy peaks at 1.2, 1.7, and 2.0 eV,[1e,16,21a,22] distinctly different from the well-characterized, slightly smaller $Au_{25}(SR)_{18}^{-1}$.

The $Au_{38}(SG)_{24}$ (SG = glutathionate) nanocluster has previously been shown to yield intense CD signals which are over five times stronger than those arising from $Au_{25}(SG)_{18}^{-}$.[24] These signals have been assigned to metal-based transitions. In fact, in light of the recent experimental[29−31] and theoretical[32,33] discoveries about core−ligand structure, the excitations labeled as "metal-based transitions" should possibly include contributions from "metal−ligand" transitions as well at the interface between the gold core and the gold−thiolate layer. Many techniques to induce chiroptical activity in MPCs have been experimentally achieved. Strong CD signals can be observed if chiral ligands are used in the synthesis of nanoparticles,[24,34,35a] if the particles are formed with achiral ligands followed by a chiral ligand-exchange reaction,[36] or from racemic solutions undergoing chiral phase transfer.[35b] However, partial ligand-exchange reactions to introduce thiolates with remote chiral centers do not lead to significant CD signals.[37] To compare different CD measurements one has to take into account that the signal can be not only temperature dependent but also solvent dependent.[35,38] The origin of the optical activity of the metal-based transitions has previously been explained by the dissymmetric field model or by a chiral ligand footprint.[35,36,38] Gold nanoparticle chirality and its origins are discussed in more detail in a recent review.[39]

The first mass-spectrometric characterization of the 8 kDa cluster in 1997 inspired early theoretical work to examine possible atomic models and structural and electronic properties of this nanoparticle.[40−43] The first studies with density functional theory (DFT) on a model cluster $Au_{38}(SR)_{24}$ examined a truncated-octahedral Au_{38} core passivated by 24 SCH_3 ligands bridging edges of the six fcc(100) facets,[40a] characterizing the surface-covalent Au−S bond to involve clear charge transfer from Au to S. Later studies considered structural motifs where the Au_{38} core is amorphous and the adsorption sites of the thiolates are irregular, finding this motif to be energetically preferable compared to the truncated-octahedral form.[41−43] In hindsight, the early DFT work suffered from the unbalance of treating the relative strengths of Au−Au and Au−S interactions reliably. Later, structural relaxations of $Au_{38}(SR)_{24}$ with improved exchange-correlation functionals lead to a drastically different structure, where a small gold core (Au_{14}) was protected from six sides by oligomeric ring-like $(AuSCH_3)_4$ units.[44] Energy comparisons to earlier models showed that, in general, the structure of thiolate-protected clusters involves competition between maximizing the metal−metal Au−Au cohesion and the optimal arrangement of the (strong) surface-covalent Au−S bonds. This energetic competition is evident by considering the bonding strength for one $RS(AuSR)_x$ ($x = 1,2$) unit to the gold core in previously discussed clusters (2−3 eV depending on x and on the charge state of the unit),[32,33,45a,55] with the calculated bond strength of the Au_2 dimer (2.2 eV, ref 45b). Discovery of "short" $[Au(SR)_2]$ and "long" $[Au_2(SR)_3]$ gold−thiolate passivating units via X-ray structure determination of $Au_{102}(p\text{-}MBA)_{44}$[29] and $Au_{25}(SCH_2CH_2Ph)_{18}^{-1}$ (refs 30 and 31) led to re-examination of $Au_{38}(SCH_3)_{24}$ as a disordered core surrounded by six short and four long motifs[46a] or three short and four long motifs.[46b] Structural principles based on numbers of short and

(25) (a) Ramakrishna, G.; Varnavski, O.; Kim, J.; Lee, D.; Goodson, T. *J. Am. Chem. Soc.* **2008**, *130*, 5032. (b) Varnavski, O.; Ramakrishna, G.; Kim, J.; Lee, D.; Goodson, T. *J. Am. Chem. Soc.* **2010**, *132*, 16. (c) Miller, S. A.; Womick, J. M.; Parker, J. F.; Murray, R. W.; Moran, A. M. *J. Phys. Chem. C* **2009**, *113*, 9440.

(26) Wang, Z. W.; Toikkanen, O.; Yin, F.; Li, Z. Y.; Quinn, B. M.; Palmer, R. E. *J. Am. Chem. Soc.* **2010**, *132*, 2854.

(27) (a) Quinn, B. M.; Liljeroth, P.; Ruiz, V.; Laaksonen, T.; Kontturi, K. *J. Am. Chem. Soc.* **2003**, *125*, 6644. (b) Toikkanen, O.; Ruiz, V.; Rönnhom, G.; Kalkkinen, N.; Liljeroth, P.; Quinn, B. M. *J. Am. Chem. Soc.* **2008**, *130*, 11049.

(28) Toikkanen, O.; Carlsson, S.; Dass, A.; Rönnholm, G.; Kalkkinen, N.; Quinn, B. M. *J. Phys. Chem. Lett.* **2010**, *1*, 32.

(29) Jadzinsky, P. D.; Calero, G.; Ackerson, C. J.; Bushnell, D. A.; Kornberg, R. D. *Science* **2007**, *318*, 430.

(30) Heaven, M. W.; Dass, A.; White, P. S.; Holt, K. M.; Murray, R. W. *J. Am. Chem. Soc.* **2008**, *130*, 3754.

(31) Zhu, M.; Aikens, C. M.; Hollander, F. J.; Schatz, G. C.; Jin, R. *J. Am. Chem. Soc.* **2008**, *130*, 5883.

(32) Akola, J.; Walter, M.; Whetten, R. L.; Häkkinen, H.; Grönbeck, H. *J. Am. Chem. Soc.* **2008**, *130*, 3756.

(33) Lopez-Acevedo, O.; Akola, J.; Whetten, R. L.; Grönbeck, H.; Häkkinen, H. *J. Phys. Chem. C* **2009**, *113*, 5035.

(34) Yanagimoto, Y.; Negishi, Y.; Fujihara, H.; Tsukuda, T. *J. Phys. Chem. B* **2006**, *110*, 11611.

(35) (a) Yao, H.; Fukui, T.; Kimura, K. *J. Phys. Chem. C* **2007**, *111*, 14968. (b) Yao, H.; Fukui, T.; Kimura, K. *J. Phys. Chem. C* **2008**, *112*, 16281.

(36) Si, S.; Gautier, C.; Boudon, J.; Taras, R.; Gladiali, S.; Bürgi, T. *J. Phys. Chem. C* **2009**, *113*, 12966.

(37) Qi, H.; Hegmann, T. *J. Am. Chem. Soc.* **2008**, *130*, 14201.

(38) (a) Noguez, C.; Garzon, I. L. *Chem. Soc. Rev.* **2009**, *38*, 757. (b) Sanchez-Castillo, A.; Noguez, C.; Garzon, I. L. *J. Am. Chem. Soc.* **2010**, *132*, 1504.

(39) Gautier, C.; Bürgi, T. *ChemPhysChem* **2009**, *10*, 483.

(40) (a) Häkkinen, H.; Barnett, R. N.; Landman, U. *Phys. Rev. Lett.* **1999**, *82*, 3264. (b) Andreoni, W.; Curioni, A.; Grönbeck, H. *Int. J. Quantum Chem.* **2000**, *80*, 598.

(41) Garzón, I. L.; Beltrán, M. R.; Posada-Amarillas, A.; Ordejón, P.; Artacho, E.; Sánchez-Portal, D.; Soler, J. M. *Phys. Rev. Lett.* **1998**, *81*, 1600.

(42) Garzón, I. L.; Michaelian, K.; Beltrán, M. R.; Posada-Amarillas, A.; Ordejón, P.; Artacho, E.; Sánchez-Portal, D.; Soler, J. M. *Eur. Phys. J. D* **1999**, *9*, 211.

(43) Garzón, I. L.; Roviera, C.; Michaelian, K.; Beltrán, M. R.; Ordejón, P.; Junquera, J.; Sánchez-Portal, D.; Artacho, E.; Soler, J. M. *Phys. Rev. Lett.* **2000**, *85*, 5250.

(44) Häkkinen, H.; Walter, M.; Grönbeck, H. *J. Phys. Chem. B* **2006**, *110*, 9927.

(45) (a) Kacprzak, K. A.; Lehtovaara, L.; Akola, J.; Lopez-Acevedo, O.; Häkkinen, H. *Phys. Chem. Chem. Phys.* **2009**, *11*, 7123. (b) Häkkinen, H.; Landman, U. *J. Am. Chem. Soc.* **2001**, *123*, 9704.

long units, core size, and number of sulfur anchors could now be made, and it was proposed that $Au_{38}(SCH_3)_{24}$ may consist of an fcc, bi-icosahedral, or bicapped Au_{25} core with nine short and two long motifs.[16] The latest structure model up to now considered a face-shared bi-icosahedral Au_{23} core surrounded by three short and six long motifs which was found to be substantially lower in energy than all the other structures in the literature.[47] This model yields an electrochemical gap which agrees with the experimental one within the inaccuracy limit of the used DFT exchange-correlation functional. However, the significant stability of the $Au_{38}(SR)_{24}$ nanocluster, its relation to the electronic structure of the gold core, and its strong chiroptical response remain to be explained.

Shell models have been shown to describe well the electronic structure and geometric shapes of metallic clusters.[48,49] Self-consistent effective potentials as well as phenomenological cluster-symmetry based potentials have been successfully proposed and utilized.[50−54] The recently proposed superatom complex (SAC) model for ligand-protected gold clusters extended the use of shell models to understand protected metallic clusters taking into account the role of the protective layer.[55] To count the delocalized electrons in the metal core, it is necessary in addition to consider the structure and the chemical nature of the ligand layer since depletion of one electron (e.g., gold−thiolate units and halide atoms),[55] two or four electrons (e.g., $Fe(CO)_4$ and $Fe(CO)_3$, respectively),[56] or zero electrons (e.g., PR_3)[55] can be realized by adsorption of ligands with varying chemical nature. The SAC model and the related orbital analysis has been very successful for several ligand-passivated gold clusters with a roughly spherical shape, accounting for their electronic stability that is due to closed electron shells composed of 8, 34, or 58 Au(6s) electrons in the gold core.[52] Furthermore, the SAC model can be used to analyze the low-lying electronic transitions that are dominantly metal-to-metal in nature in the core. For elongated systems such as nanorods, the ellipsoidal shell model or the particle-in-a-cylinder (PIC) model[49b,50−52] may be employed to explain the observed electronic shell closings. Applying the established electron counting rules,[55] the $Au_{38}(SR)_{24}$ cluster has 14 delocalized electrons in a core that is strongly prolate-deformed (cigar-like or a nanorod). It can be noted that as the closest electron shell closures in a spherical system occur at 18 or 20 electrons, a 14-electron system has partially filled degenerate orbitals if the cluster shape is spherical. Consequently, an s-metal cluster with 14 atoms is expected to deform strongly by the Jahn−Teller mechanism, as indeed observed in DFT molecular dynamics simulations of neutral Na_{14}.[53c]

Here, we investigate the atomic and electronic structure as well as optical absorption and circular dichroism of $Au_{38}(SR)_{24}$ via DFT computations. We have identified a large number of energetically low-lying structures and found several that are preferred over the current "state-of-the-art" structural model (ref 47). The computed structure factor of powder X-ray diffraction (XRD) of our lowest energy conformers of $Au_{38}(SCH_3)_{24}$ and $Au_{38}(SC_6H_{13})_{24}$ match remarkably well with the experimental one, obtained and reported here for the first time from a high-purity sample of $Au_{38}(SC_{12}H_{25})_{24}$. The lowest-energy isomer found here has an intrinsically chiral structure due to special arrangement of the protective $SR(AuSR)_x$ units on the surface of its Au_{23} core. The computed absorption and CD spectrum of the lowest energy structure of $Au_{38}(SCH_3)_{24}$ matches with the measured one for $Au_{38}(SG)_{24}$ (ref 24) quantitatively in the low-energy excitation (NIR−visible light) range. We identify the strong optical transitions and the chiral response in the context of a particle-in-a-cylinder model. The combined computational and experimental structural characterization of the $Au_{38}(SR)_{24}$ cluster, presented here, is rather complete and may aid further understanding of this much-studied nanocluster in lieu of the single-crystal X-ray structure determination.

Experimental Section

Details of a synthesis of $Au_{38}(SC_{12}H_{25})_{24}$ clusters have been described in ref 16. Briefly, the crude mixture of dodecanethiolate-protected Au clusters was prepared by the Brust method[57] and was incubated at 353 K in a neat solution of dodecanethiol to enhance the population of magic clusters. The $Au_{38}(SC_{12}H_{25})_{24}$ clusters were extracted from the incubated clusters with the mixed solvent of toluene and acetone with a volume ratio of 1:4. The purity of the sample was confirmed by mass spectrometry and optical spectroscopy.

The $Au_{38}(SC_{12}H_{25})_{24}$ sample in the powder form was filled into a capillary ($\phi = 0.5$ mm) made of borosilicate glass and X-ray powder diffraction was measured with the high-resolution powder diffractometer on beamline BL44B2 ($\lambda = 0.5529$ Å) at SPring-8. The powder XRD pattern of $Au_{38}(SC_{12}H_{25})_{24}$ presented in this paper was obtained after subtracting the contribution of the glass capillary.

Computational Methods

Energy calculations and structure optimizations are performed using the real-space finite-difference DFT code GPAW.[58] We use the outermost 11, 6, and 4 electrons as valence for Au, S, and C, respectively. GPAW makes use of the all-electron density, where the electrons are described using the projector augmented wave (PAW) method in the frozen core approximation.[59] The PAW setup for the Au($5d^{10}6s^1$) valence configuration includes scalar-relativistic effects. Exchange and correlation effects are included through the Perdew, Burke, and Ernzerhof (PBE) energy functional.[60] The Kohn−Sham wave functions are expanded directly on a real space grid with a grid spacing of 0.2 Å. Optimizations of the considered structures have been performed until the maximal force is below

(46) (a) Jiang, D.-e.; Tiago, M.; Luo, W.; Dai, S. *J. Am. Chem. Soc.* **2008**, *130*, 2777. (b) Jiang, D.-e.; Luo, W.; Tiago, M. L.; Dai, S. *J. Phys. Chem. C* **2008**, *112*, 13905.
(47) Pei, Y.; Gao, Y.; Zeng, X. C. *J. Am. Chem. Soc.* **2008**, *130*, 7830.
(48) (a) de Heer, W. A. *Rev. Mod. Phys.* **1993**, *65*, 611. (b) Brack, M. *Rev. Mod. Phys.* **1993**, *65*, 677.
(49) (a) Knight, W. D.; Clemenger, K.; de Heer, W. A.; Saunders, A.; Chou, M. Y.; Cohen, M. L. *Phys. Rev. Lett.* **1984**, *52*, 2141. (b) Clemenger, K. *Phys. Rev. B* **1985**, *32*, 1359.
(50) Kraus, W. A.; Schatz, G. C. *J. Chem. Phys.* **1983**, *79*, 6130.
(51) Sun, J.; Buhro, W. E.; Wang, L.-W.; Schrier, J. *Nano Lett.* **2008**, *8*, 2913.
(52) Johnson, H. E.; Aikens, C. M. *J. Phys. Chem. A* **2009**, *113*, 4445.
(53) (a) Koskinen, M.; Lipas, P. O.; Manninen, M. *Z. Phys. D* **1995**, *35*, 285. (b) Häkkinen, H.; Kolehmainen, J.; Koskinen, M.; Lipas, P. O.; Manninen, M. *Phys. Rev. Lett.* **1997**, *78*, 1034. (c) Häkkinen, H.; Manninen, M. *Phys. Rev. B* **1995**, *52*, 1540. (d) Reimann, S. M.; Koskinen, M.; Häkkinen, H.; Lindelof, P. E.; Manninen, M. *Phys. Rev. B* **1997**, *56*, 12147.
(54) Bonačić-Koutecký, V.; Fantucci, V. P.; Koutecky, J. *Phys. Rev. B* **1988**, *37*, 4369.
(55) Walter, M.; Akola, J.; Lopez-Acevedo, O.; Jadzinsky, P. D.; Calero, G.; Ackerson, C. J.; Whetten, R. L.; Grönbeck, H.; Häkkinen, H. *Proc. Natl. Acad. Sci. U.S.A.* **2008**, *105*, 9157. (b) Häkkinen, H. *Chem. Soc. Rev.* **2008**, *37*, 1847.
(56) Lopez-Acevedo, O.; Rintala, J.; Virtanen, S.; Femoni, C.; Tiozzo, C.; Grönbeck, H.; Pettersson, M.; Häkkinen, H. *J. Am. Chem. Soc.* **2009**, *131*, 12573.
(57) Brust, M.; Fink, J.; Bethell, D.; Schiffrin, D. J.; Kiely, C. *J. Chem. Soc., Chem. Commun.* **1995**, 1655.
(58) Mortensen, J. J.; Hansen, L. B.; Jacobsen, K. W. *Phys. Rev. B* **2005**, *71*, 035109.
(59) Blöchl, P. E. *Phys. Rev. B* **2009**, *80*, 195112.
(60) Perdew, J. P.; Burke, K.; Ernzerhof, M. *Phys. Rev. Lett.* **1996**, *77*, 3865.

0.05 eV/Å on any atom. The estimated mean error for the PBE functional when comparing atomization energies of small molecules to their experimental values is 0.3 eV.[61] Molecular graphics images were produced using the UCSF Chimera package.[62,63]

Theoretical XRD intensities are obtained, within a classical description of the scattering process, using the Debye formula:[64]

$$I(s) \propto \sum_{i<j} Z_i Z_j \frac{\sin(2\pi s r_{ij})}{2\pi s r_{ij}}$$
$$s = \frac{2 \sin\theta}{\lambda}$$

where i,j are atom indexes, Z_i is the atomic number of atom i, r_{ij} is the corresponding interatomic distance, and θ is the scattering angle.

The Amsterdam Density Functional (ADF) program[65] is used for optical absorption and circular dichroism calculations in addition to geometry optimizations with the Xα functional. The Xα functional has previously been shown to lead to accurate Au−Au core distances in the $Au_{25}(SR)_{18}^{-1}$ nanoparticle.[66] In the ADF calculations, scalar relativistic effects are included by utilizing the zeroth-order regular approximation (ZORA).[67] The Slater type basis sets employed in the Xα geometry optimizations are of polarized triple-ζ (TZP) quality with a [$1s^2$-$4f^{14}$] frozen core for Au, a [$1s^2$-$2p^6$] frozen core for S, and a [$1s^2$] frozen core for C. The energy convergence criterion is tightened to 10^{-4}, and the gradient convergence criterion is tightened to 10^{-3}. The PBE exchange functional is utilized in time-dependent density functional theory (TDDFT) computations to determine energetics, oscillator strengths, and compositions of excited states. Orbitals are plotted using the ADF-GUI program with a contour value of 0.0175. A frozen core double-ζ (DZ) basis set for gold and double-ζ plus polarization (DZP) basis sets for all other elements are utilized in the TDDFT calculations. Rotatory strengths are computed using the RESPONSE module in ADF.[68] For the rest of this section all the units are cgs units. The computed rotatory strengths R are in units of $esu^2\ cm^2$. To simulate the spectrum in the experimental units of 10^{-3} L cm^{-1} mol^{-1} (often reported as millidegrees or mdeg) the following factor is used:[69,70]

$$\alpha = \frac{4\pi^2 N_A}{3\ln(10)10^3} \frac{2\pi}{hc}$$

where N_A is Avogadro's number, h is Planck's constant, and c is the speed of light. The absorption and circular dichroism spectra are obtained by summing folded dipole moments and oscillatory strengths with excitation number m. We use a scaled Gaussian function sigma with a width at half-maximum corresponding to 0.1 eV as

$$\varepsilon(E) = \alpha \sum_m d_m^2 E_m \sigma_m(E)$$
$$\Delta\varepsilon(E) = 4\alpha \sum_m R_m E_m \sigma_m(E)$$

Results and Discussion

Geometric Structure and Energetics. As discussed in the introduction, a bi-icosahedral Au_{23} core consisting of two icosahedral Au_{13} units fused at a 3-fold face has previously been determined to lead to a low energy isomer for $Au_{38}(SR)_{24}$.[47] Although the structure described in ref 47 is quite stable relative to isomers with different core structures, a number of lower energy geometries have been found in this work, regarding the structure of the protective gold−thiolate layer. The structure of this layer is crucial with respect to chirality. As in ref 47, the idealized Au_{23} core has D_{3h} symmetry. This core can be covered with six long [$Au_2(SR)_3$] and three short [$Au(SR)_2$] units, where the long units protect the high-curvature ends of the Au_{23} core and the short units passivate the low-curvature center. Placement of one long unit connecting atoms A and C (Figure 1a) dictates the arrangement of two other long units around the 3-fold longitudinal axis. However, the three long units on the other high-curvature end of the Au_{23} core can be related to the first three units by either a mirror plane (which would connect atoms A′ and C′ in Figure 1a) or a C_2 axis (connecting atoms A″ and C″); these arrangements lead to isomers with C_{3h} or D_3 symmetry, respectively (Figure 1b and 1c). The short units are attached to symmetry-equivalent atoms B and B′. The possibility of two ligand arrangements in the $Au_{38}(SR)_{24}$ nanoparticle differs from the case of $Au_{25}(SR)_{18}$ and $Au_{144}(SR)_{60}$ where attachment of one ligand determines the relative arrangement of the remaining ligands.[33]

Both the C_{3h} and D_3 isomers possess only four unique SR groups (three on a long unit and one on a short unit); all other SR groups are related by symmetry transformations. Due to steric considerations, eight conformers obtained by inversion of the CH_3 groups through the Au−S−Au plane are possible for both high symmetry systems. It should be noted that the orientation of the organic groups does not need to preserve C_{3h} or D_3 symmetry; for instance in the structure described in ref 47, the long units are arranged in an idealized C_{3h} symmetry but the asymmetrical location of the methyl groups leads to C_1 symmetry for the nanocluster.

The relative energies of the eight D_3 and the eight C_{3h} conformers as well as the structure reported in ref 47 are displayed in Table 1 for the Xα and PBE levels of theory. The geometry convergence precision of the energies reported in Table 1 are approximately 0.01 eV for Xα. Symmetry constraints were employed in the Xα optimizations, whereas no constraints were used in the PBE relaxations. The structures are numbered according to increasing energy calculated with the Xα functional (structures **1**−**8** belonging to the D_3 isomer family and **9**−**17** to the C_{3h} family, **9** being the structure reported in ref 47). As shown in Table 1, conformers with a D_3 ligand arrangement are in general lower in energy than those with a C_{3h} arrangement. The four lowest-energy D_3 structures **1**−**4** are 0.35−0.71 eV lower in energy with the Xα functional or 0.26−0.34 eV lower in energy with the PBE functional than the C_{3h}-based structure **9**. Using the PBE functional, **9** is at least 0.11 eV (0.28 eV with the Xα functional) lower in energy than the pure C_{3h} structures **10**−**17**, which suggests that the methyl group orientation is not sterically ideal in the highly symmetric

(61) Staroverov, V. N.; Scuseria, G. E.; Tao, J.; Perdew, J. P. *J. Chem. Phys.* **2004**, *121*, 11507.
(62) Pettersen, E. F.; Goddard, T. D.; Huang, C. C.; Couch, G. S.; Greenblatt, D. M.; Meng, E. C.; Ferrin, T. E. *J. Comput. Chem.* **2004**, *13*, 1605.
(63) http://www.cgl.ucsf.edu/chimera.
(64) Azároff, L. V. *Elements of X-ray Crystallography*; McGraw-Hill: 1968.
(65) te Velde, G.; Bickelhaupt, F. M.; Baerends, E. J.; Fonseca Guerra, C.; van Gisbergen, S. J. A.; Snijders, J. G.; Ziegler, T. *J. Comput. Chem.* **2001**, *22*, 931.
(66) Aikens, C. M. *J. Phys. Chem. A* **2009**, *113*, 10811.
(67) van Lenthe, E.; Baerends, E. J.; Snijders, J. G. *J. Chem. Phys.* **1993**, *99*, 4597.
(68) Autschbach, J.; Ziegler, T.; Gisbergen, S. J. A.; Baerends, E. J. *J. Chem. Phys.* **2002**, *116*, 6930.
(69) Koslowski, A.; Sreerama, N.; Woody, R. W. In *Circular Dichroism: Principles and Applications*, 2nd ed.; Berova, N., Nakanishi, K., Woody, R. W., Eds.; Wiley-VCH: New York, 2000.
(70) Schellman, J. A. *Chem. Rev.* **1974**, *75*, 323.

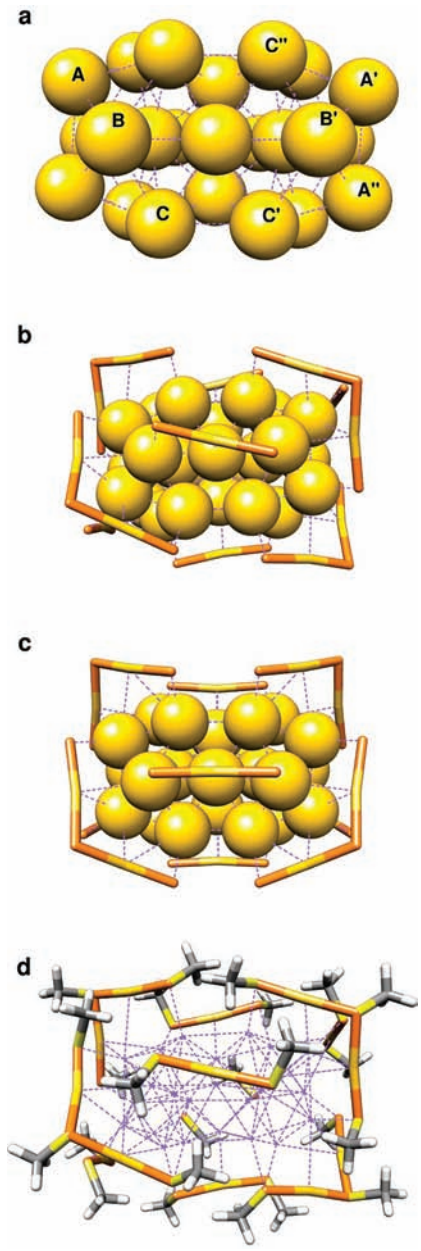

Figure 1. (a) Au_{23} core with labeling of the surface Au atoms involved in determining the symmetry of the ligand layer. (b) Chiral D_3 arrangement of the Au−S atoms. (c) C_{3h} arrangement of the Au−S atoms. (d) Optimal SCH_3 distribution on structure **1**.

C_{3h} systems. As a consequence of symmetry, all of the short units in the D_3 structures are arranged so that the methyl groups are in a trans configuration, whereas in the C_{3h} structures these units have a cis orientation; in structure **9**, the short units contain a mixture of trans and cis arrangements. In D_3 structure **1**, all of the methyl groups in both long and short units are arranged in trans orientations. The zigzag features from neighboring units form "barber-pole" stripes around the nanoparticle (Figure 1d). For the D_3 structures, the lowest energy systems tend to have the least methyl group congestion. For example, D_3 structures **1**, **2**, **4**, and **6** do not have methyl groups pointing into the C_3 axis. It should be noted that conformers **1**−**4** are of similar energy, which agrees with the generally accepted statement that changes in the conformation around the S atoms involve small energy differences. However, D_3 conformers **5**−**8** and C_{3h} conformers **12**−**17** lie significantly above the lowest energy conformer for each symmetry.

Table 1. Relative Energies of Relaxed D_3 and C_{3h} Structures[a]

Structure	Symmetry	Xα Energy (eV)	PBE Energy (eV)
1	D_3	0.00	0.00
2	D_3	0.21	0.06
3	D_3	0.32	−0.08
4	D_3	0.36	0.00
5	D_3	0.66	0.47
6	D_3	0.73	0.31
7	D_3	0.82	0.36
8	D_3	1.33[b]	0.44
9 (ref 47)	C_1 (C_{3h}-based)	0.71	0.26
10	C_{3h}	0.99	0.37
11	C_{3h}	1.22	0.65
12	C_{3h}	2.09	1.08
13	C_{3h}	2.31	1.20
14	C_{3h}	2.31	1.02
15	C_{3h}	2.38	1.14
16	C_{3h}	2.53[b]	1.26
17	C_{3h}	3.32[b]	1.52

[a] The PBE relaxation used no symmetry constraints. [b] Loose optimization criteria used.

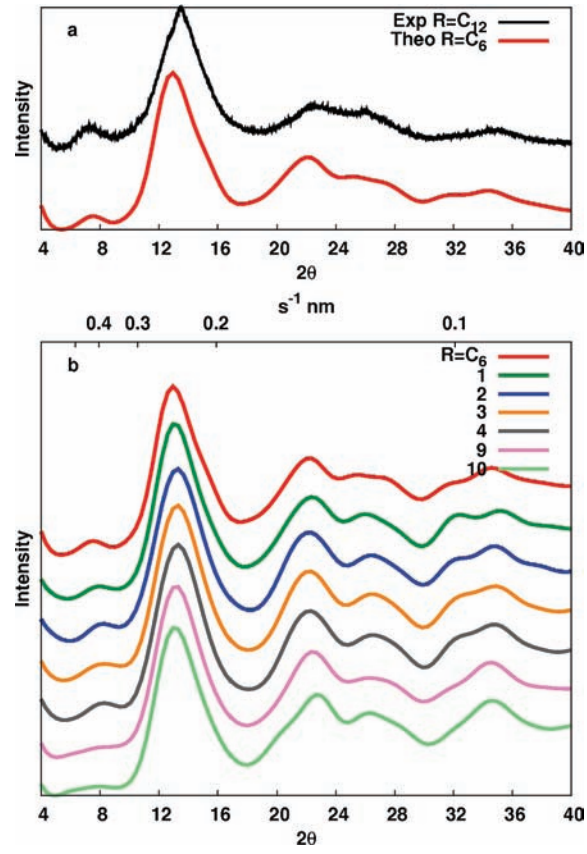

Figure 2. (a) Experimental XRD pattern. Comparison to calculated XRD for structure **1** with R = C_6H_{13} show an excellent agreement. An exponential thermal damping factor[32] with $\beta = 0.1$ nm^2 is used. (b) XRD calculated intensities shown as a function of experimental measured angle 2θ for low energy theoretical structures. The Debye formula is used with no thermal factor correction.

XRD. The experimental XRD pattern for $Au_{38}(SC_{12}H_{25})_{24}$ and the theoretical XRD pattern for a relaxed $Au_{38}(SC_6H_{13})_{24}$ structure with the ligand arrangement of conformer **1** of $Au_{38}(SCH_3)_{24}$ (denoted **1** R = C6) are displayed in Figure 2a. Figure 2b presents the theoretical XRD intensities as a function

of the measured angle (2θ) (lower x axis) and the s^{-1} variable (upper x axis) for the four lowest-energy D_3 structures **1**−**4**, structure **9**, and the lowest energy C_{3h} structure **10**. The XRD patterns for all relaxed structures are shown in the Supporting Information (Figure S1). The relaxed $Au_{38}(SC_6H_{13})_{24}$ structure is displayed in Figure S2. The first peak observed in the experimental pattern (Figure 2a) at $s^{-1} > 0.4$ nm is clearly obtained in the patterns of **1**−**4** and is present with low intensity in the XRD patterns of **9** and **10**. This general trend holds true for all D_3 and C_{3h} structures (Figure S1), which suggests that this peak is symmetry related. As the first peak corresponds to the second neighbor distances (Au−Au and Au−S), it can be interpreted as a sign of a more long-range ordered D_3 structure with respect to C_{3h}. It should be noted that this peak overlaps with the diffraction of amorphous silicon of a glass capillary used in the synchrotron experiments (Figure S3), so a quantitative analysis of this peak is not possible.

The second and most intense peak is slightly shifted toward bigger s^{-1} with respect to the equivalent experimental peak, which is expected from PBE overestimation of the Au−Au bond length. Diffraction in the smaller s^{-1} range may correspond to higher order diffractions such as (220), (311), etc. and has in general good agreement. Depending on the structure, slight differences can be noted in the peaks near $2\theta = 25°-28°$ and $2\theta = 31°-34°$. Overall, the XRD pattern of the four lowest-energy D_3 conformers agrees very well with the experimental XRD pattern.

Electronic Structure. The electronic structure of the prolate D_3 and C_{3h} isomers can be analyzed by considering a nanorod-like particle-in-a-cylinder (PIC) model; other idealized models are presented in the Supporting Information. Throughout the current and subsequent sections, "core" refers to the Au_{23} core and "ligands" refer to the gold−thiolate passivating units. The core of $Au_{38}(SCH_3)_{24}$ has characteristics of nanorods such as a set of degenerate transverse axes that are shorter than the longitudinal axis. The electronic structure of the nanocluster reflects this symmetry; as shown in Figure 3 for **1**, the occupied and unoccupied orbitals near the HOMO−LUMO gap have Σ, Π, and Δ symmetries similar to those observed previously for pentagonal silver nanorods.[52] These orbitals are labeled M_l, where the azimuthal quantum number $M = 0, 1, 2, ...$ corresponds to Σ, Π, Δ, ... orbitals and $l = 1, 2, 3, ...$ corresponds to the axial quantum number. Degenerate orbitals such as Π, Δ, and HOMO-4 are also labeled "a" or "b", where "a" represents an orbital that is symmetric with respect to the C_2 axis. The energies predicted with the PIC model for a slightly elongated nanorod (see Supporting Information) correspond well with the energy level diagram shown in Figure 3. Due to the presence of ligand-based orbitals and Au 5d-band orbitals, the Σ_1 and Σ_2 orbitals lie much lower in energy than would be predicted by a PIC model (around −8.0 eV in Figure 4). In addition, ligand-based orbitals such as HOMO-4 − HOMO-6 naturally do not conform to the straightforward PIC model. However, the PIC model provides a useful basis for understanding the optical absorption spectra of these systems.

The projection on local atomic basis (Figure 4) shows in the region from −2 to 0 eV (HOMO) a mixed nature of orbitals. This is found systematically in all other thiolate protected clusters and is not dependent on the particular core symmetry. In addition to the expected core metal orbitals (5d and 6sp) Au−S ligand based orbitals are also present. Therefore the optical excitations in the lower energy range (roughly 1 eV above the optical gap) can be expected to be originating not only from the metallic core but also from the ligand layer. As shown in Figure 4, the local electronic structure (signified by the atom-projected local density of electron states, PLDOS) of the Au atoms is different for the atoms in the core and in the ligand shell. Based on this difference one can without ambiguity classify our new structures as belonging to the "Divide and Protect" structural motif first discussed in ref 44.

The electronic structure and orbitals of **9** are similar to those of structure **1**, with Σ, Π, and Δ-like symmetry in the delocalized orbitals near the HOMO−LUMO gap. The Π and Δ orbitals are slightly split in energy (Figure S6) due to symmetry-lowering. The HOMO-3 and lower energy orbitals are ligand-based. The Δ_2 symmetry in the LUMO+3 is more evident than in **1** (Figure S7).

Optical Absorption Spectra. In general, the strong transitions observed in the optical absorption spectrum agree well with the interpretation of $Au_{38}(SR)_{24}$ as a nanorod. Due to the symmetry of these transitions, experiments could be designed to selectively measure either the transverse or longitudinal excitations. In the PIC model, the strongest longitudinal transitions should arise when $\Delta M = 0$ and Δl is odd. Similarly, the most intense transverse transitions should occur when $\Delta M = \pm 1$ and $\Delta l = 0$. The optical absorption spectra of structures **1** and **9** are compared in Figure 5. Both spectra exhibit four main peaks, in agreement with the previous theoretical spectrum of structure **9** from ref 47. Here we discuss in detail the transitions labeled a−d for **1** in Figure 5. The first peak (a) at 1.01 eV is predicted to arise from the HOMO→LUMO ($\Pi_2 \rightarrow \Pi_3$) transition, as shown in Table S2. No HOMO→LUMO+1 ($\Pi_2 \rightarrow \Sigma_4$) excitation is evident. In addition, the HOMO→LUMO+2 ($\Pi_2 \rightarrow \Delta_1$) transition at 1.22−1.26 eV is weak, with oscillator strengths less than 0.0012. Peak b at 1.33−1.36 eV primarily arises from transitions out of the HOMO−1 and HOMO−2 into the LUMO (($\Sigma_3 \rightarrow \Pi_3$) and ($\Pi_1 \rightarrow \Pi_3$), respectively). Although the weight of the $\Pi_1 \rightarrow \Pi_3$ transition in this excitation is large, the actual contribution to the transition dipole moment is small, which corresponds with the forbidden transition in the PIC model.

The six strong excitations that lie in the 1.59−1.72 eV range comprising peak c arise from a combination of several transitions including HOMO−1→LUMO+1 ($\Sigma_3 \rightarrow \Sigma_4$), HOMO−2→LUMO+2 ($\Pi_1 \rightarrow \Delta_1$), and HOMO−3→LUMO (ligand→Π_3). In particular, the strong peak at 1.59 eV is primarily composed of the $\Sigma_3 \rightarrow \Sigma_4$ transition. Peak d at 1.90−1.95 eV is quite mixed, with contributions from HOMO→LUMO+3 as well as transitions into the LUMO from ligand orbitals (HOMO-4 − HOMO-6). For this peak, the ligand→LUMO transitions (especially HOMO-6→LUMO) contribute the most to the overall transition dipole moment.

For structure **9**, the first peak at 1.02 eV also arises from the HOMO→LUMO ($\Pi_2 \rightarrow \Pi_3$) transition (Table S3). A weak peak at 1.22−1.23 eV comes from the HOMO→LUMO+1 ($\Pi_2 \rightarrow \Sigma_4$) transition due to the lower symmetry of this system, but this excitation is still essentially forbidden. As for **1**, the broad peak from 1.28 to 1.43 eV arises from a combination of HOMO→LUMO+2 ($\Pi_2 \rightarrow \Delta_1$) and transitions from the HOMO−1 and HOMO−2 into the LUMO (($\Sigma_3 \rightarrow \Pi_3$) and ($\Pi_1 \rightarrow \Pi_3$), respectively). Peak c from 1.66−1.85 eV is much broader than the corresponding peak for **1** and is composed from transitions out of the HOMO−1 and HOMO−2 into the LUMO+1 and LUMO+2, from HOMO to LUMO+3, and from ligand orbitals into the LUMO. Peak d (1.89−2.01 eV) arises from excitations out of lower energy ligand orbitals in addition to HOMO→LUMO+3 and HOMO→LUMO+4.

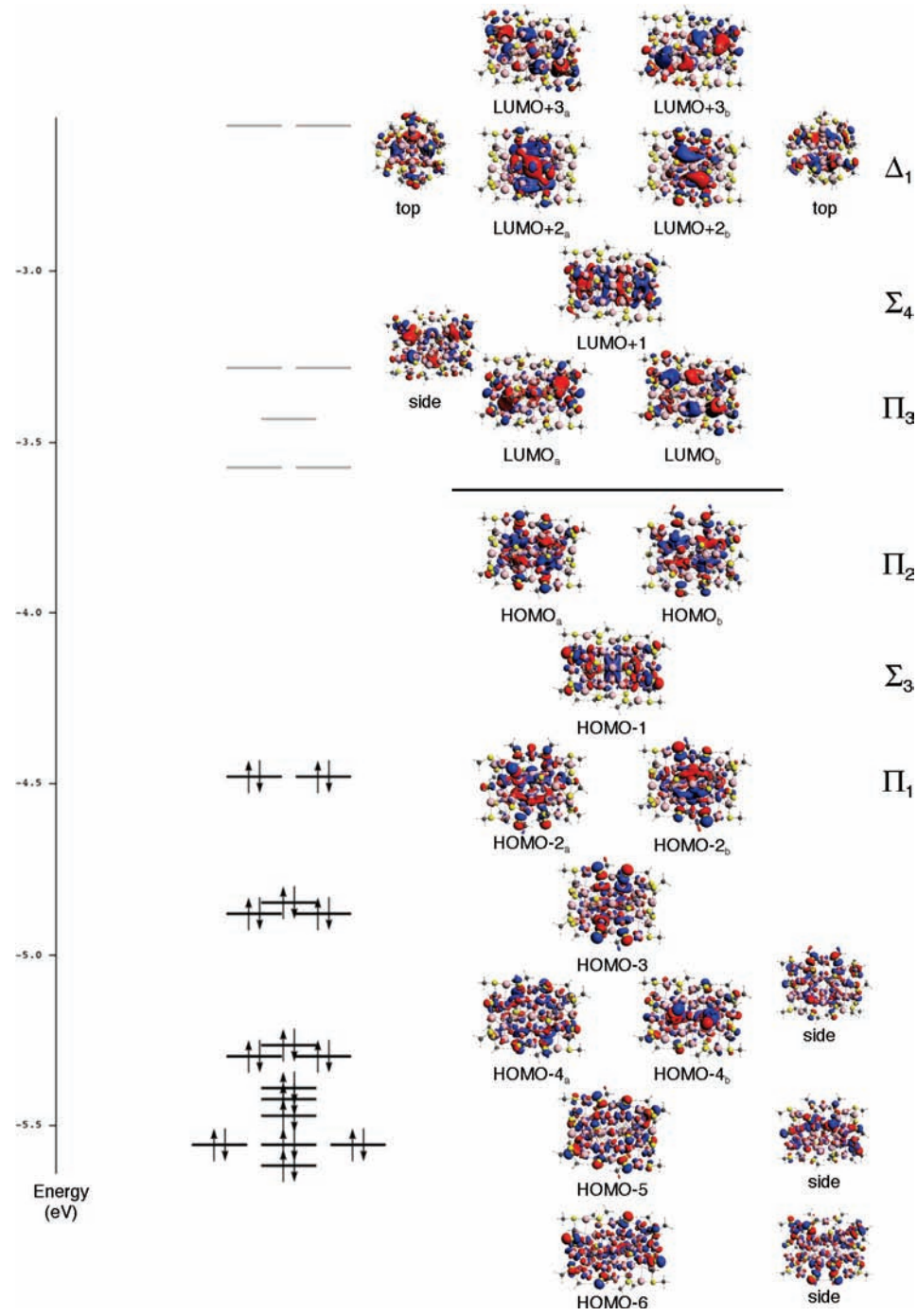

Figure 3. PBE Kohn−Sham orbitals and energy level diagram for structure **1**.

Circular Dichroism Spectra. The circular dichroism spectra for **1** and **9** are compared in Figure 6. For both structures, the HOMO→LUMO transition has a moderately negative rotatory strength ($R = -48.3 \times 10^{-40}$ esu^2 cm^2 for **1** or -70.3×10^{-40} esu^2 cm^2 for **9**). The transitions comprising peak b have positive rotatory strengths for both structures. Differences between the structures are evident in peaks c and d. In structure **1**, states 21, 22, 26, and 27 have large negative rotatory strengths ((-44.5 to -135.7) $\times 10^{-40}$ esu^2 cm^2) while states 24 and 25 have large positive rotatory strengths (($+65.6$ to $+84.3$) $\times 10^{-40}$ esu^2 cm^2). The folded spectrum for peak c is decidedly negative. In structure **9**, the magnitudes of the rotatory strengths are much smaller ($|R| \leq 22.0 \times 10^{-40}$ esu^2 cm^2) and the overall envelope of the peak is slightly negative. Peak d for **1** is dominated by state 44, which has a rotatory strength of $+347.4 \times 10^{-40}$ esu^2 cm^2. This peak has a strong contribution from transitions out of the ligand-based orbitals, which suggests that the chiral distribution of the protecting ligands may significantly enhance the rotatory strengths of excitations involving these orbitals. In contrast, peak d for **9** is moderately negative and is not dominated by a single state. Overall, the CD signals of the system with higher chiral symmetry (structure **1**, D_3) are more intense than those for the system with no symmetry (structure **9**, C_1). This behavior has previously been observed for phosphine-stabilized Au_{11} clusters, in which the CD signals predicted

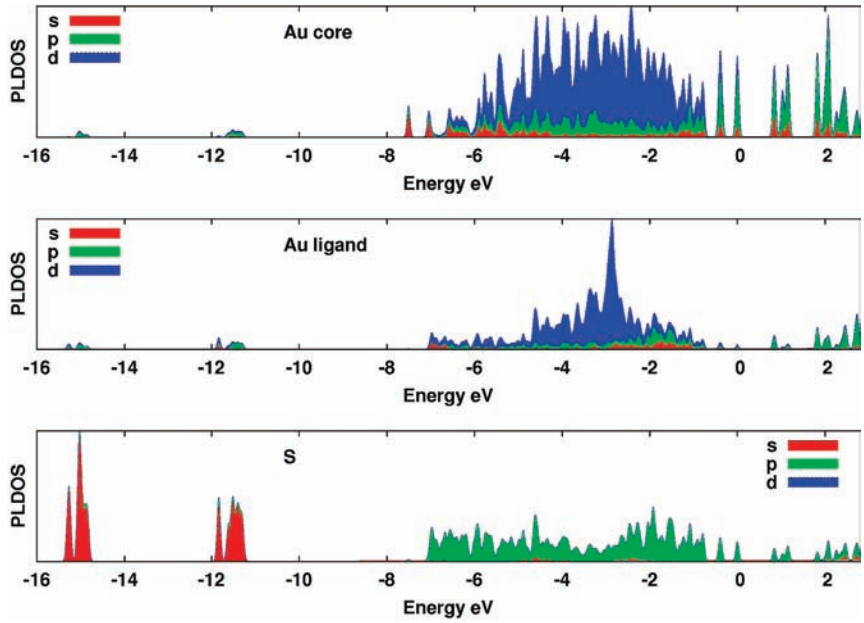

Figure 4. Structure **1** density of states projected on local atomic basis (PLDOS) and separated by type of atoms: (a) core Au_{23} atoms; (b) Au atoms in "short" $Au(SR)_2$ and "long" $Au_2(SR)_3$ gold−thiolate passivating units; (c) S atoms.

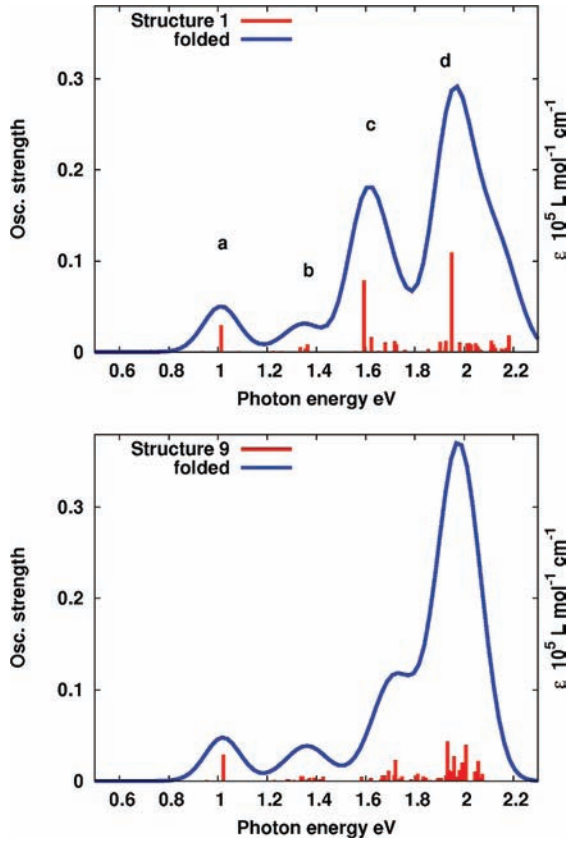

Figure 5. Calculated LR-TDDFT oscillator strength and optical absorption spectrum of structures **1** and **9**.

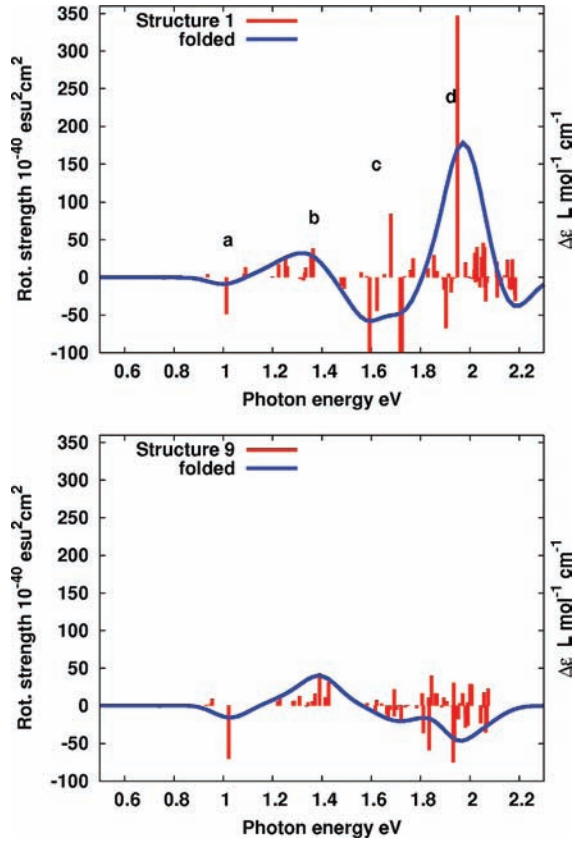

Figure 6. Calculated LR-TDDFT rotatory strength and CD spectrum of structures **1** and **9**.

for a structure with a C_2 core are approximately a factor of 2 larger than those for a similar structure with a C_1 core.[71]

In the published experimental CD spectrum for $Au_{38}(SG)_{24}$,[24] peaks below 1.3 eV are outside the wavelength range of the instrument. The first negative peak appears at 1.6 eV with a $\Delta\epsilon$ value of approximately -12 L mol^{-1} cm^{-1}, in good agreement with peak c of **1**, which has a maximum at 1.6 eV and a shoulder at 1.7 eV and has a predicted folded $\Delta\epsilon$ value of approximately -60 L mol^{-1} cm^{-1}. The first positive peak in the experimental spectrum falls just below 2 eV with a $\Delta\epsilon$ value of approximately 30 L mol^{-1} cm^{-1}; this correlates well to peak d of **1**, which has a maximum at 1.97 eV with a folded $\Delta\epsilon$ value of 180 L mol^{-1}

(71) Provorse, M. R.; Aikens, C. M. *J. Am. Chem. Soc.* **2010**, *132*, 1302.

cm^{-1}. The positions of these two peaks are extremely well-reproduced in the theoretical calculations, and the intensities are off by a factor of 5−6. The differences in intensities could be due in part to factors such as temperature or solvent; they would respectively enter in the simulated spectra as a bigger Gaussian width and a term depending on the refractive index n here set to 1.[69,70] For instance a half-width of 0.3 eV instead of 0.1 eV would reduce the intensity by a factor of 3 (not shown).

Conclusions

Our joint computational and experimental investigation of the structural properties of the $Au_{38}(SR)_{24}$ nanocluster has identified a new low-energy, chiral, D_3 symmetric structure that yields an excellent match between computed (for $R = C_6H_{13}$) and measured (for $R = C_{12}H_{25}$) powder XRD function. We have characterized the electronic shell structure of this nanocluster in terms of a particle-in-a-cylinder model. While the linear absorption spectrum of the new structure is not distinctive as compared to the ones for previous candidates for low-energy structures, the CD response in the low-energy region (below 2.2 eV) of the new structure is very similar to the one reported several years ago from experiments for $Au_{38}(SG)_{24}$. The mechanism of the chiral response for low excitation energies is related to the chiral arrangement of the gold−thiolate ligand shell around the bi-icosahedral Au_{23} core. This mechanism is qualitatively different from the one reported from a recent theoretical study of $Au_{25}(SR)_{18}^{-1}$ clusters[38b] and can be expected to be present also for the larger thiolate-protected clusters $Au_{102}(SR)_{44}$ and $Au_{144}(SR)_{60}$, where nonchiral Au cores are protected by a chiral arrangement of gold−thiolate units.[29,33,52]

Acknowledgment. The authors thank Risako Tsunoyama for preparing the $Au_{38}(SC_{12}H_{25})_{24}$ sample used in this work and Jaakko Akola for discussions. The XRD measurements were performed at the beamline (BL44B2) of RIKEN Materials Science in SPring-8 with the approval of RIKEN (Proposal No. 20090055) with support by Dr. Kenichi Kato and Prof. Masaki Takata. C.M.A. thanks the Air Force Office of Scientific Research (AFOSR) and the Defense Advanced Research Projects Agency (DARPA) for financial support under Award FA9550-09-1-0451. H.H. thanks the Academy of Finland for financial support. The computational resources were provided by the CSC − the Finnish IT Center for Science in Espoo, Finland.

Supporting Information Available: Theoretical XRD spectra of structures **1**−**17**. Calculated structure of $Au_{38}(SC_6H_{13})_{24}$. Particle-in-a-cylinder and model potential analysis. Excited state transitions, oscillator strengths, rotatory strengths, and LUMO+3 orbitals for structures **1** and **9**. PBE coordinates for structures **1**−**4**. This material is available free of charge via the Internet at http://pubs.acs.org.

JA102934Q